Journal of Water Process Engineering 70 (2025) 107003

Contents lists available at ScienceDirect

Journal of Water Process Engineering

journal homepage: www.elsevier.com/locate/jwpe

Rice husk silica derived MICROSCAFS® for a green solar-driven photodegradation of minocycline in aqueous media

Francesca Langiano [a], Sofia Moreira Fernandes [b], Beatriz Trindade Barrocas [b], Anna Del Tedesco [a], Pietro Riello [a], Maria João Ferreira [c], Ana C. Marques [b], Massimo Sgarzi [a], Matteo Gigli [a,*], Claudia Crestini [a]

[a] Department of Molecular Sciences and Nanosystems, Ca' Foscari University of Venice, Via Torino 155, 30172 Venice, Italy
[b] CERENA, DEQ, Instituto Superior Técnico, Universidade de Lisboa, Av. Rovisco Pais, 1049–001 Lisboa, Portugal
[c] Centro de Química Estrutural (CQE), Instituto Superior Técnico, Universidade de Lisboa, Av. Rovisco Pais, 1049-001 Lisboa, Portugal

ARTICLE INFO

Editor: Xiaying Xin

Keywords:
Rice husk
Porous silica microspheres
Sol-gel
Minocycline
Water treatment
Photocatalysis
Antibiotic removal

ABSTRACT

The increasing consumption of antibiotics is causing the rise of multidrug-resistant bacterial strains. Therefore, the removal of these molecules from water is highly important and requires the development of high-performance systems, whose production from biobased resources, especially residues, would greatly enhance their sustainability value. This work focuses on the development of TiO_2-containing porous silica microspheres, MICROSCAFS®, using rice husk as silica source. The MICROSCAFS® are employed in the adsorption and solar-driven photodegradation of minocycline, a ubiquitous antibiotic for various therapies. The biobased content of the MICROSCAFS® is increased by substituting tetraethyl orthosilicate, commonly employed for their preparation, with rice husk-extracted silica. The incorporation of biogenic silica alters the structure of MICROSCAFS®, that display a hollow structure with high surface porosity. Furthermore, upon high temperature treatment, a significant increase in surface area, up to ca. 92 $m^2 \bullet g^{-1}$ is observed, leading to an adsorption capacity of 80.81 $mg \bullet g^{-1}$. The adsorption mechanism is best described by the Freundlich model, implying that adsorbate multilayers are formed during the process. The presence of 3.4 nm anatase crystallites confers an efficient photocatalytic ability ($k = 7.6 \bullet 10^{-2}$ $mg \bullet L^{-1} \bullet min^{-1}$) to the biobased MICROSCAFS®, yielding a complete removal of minocycline (10 $mg \bullet L^{-1}$ in simple water matrices and adsorbent dosage of 50 mg) via a 45-minute irradiation in solar-simulated conditions (1 sun) compared to 165 min needed for fossil-based MICROSCAFS®. Zero-order kinetics best fit the process, the rate limiting step being the photodegradation reaction. Lastly, the high rate of photodegradation is maintained over 4 cycles, demonstrating the high system stability.

1. Introduction

The relentless pace of industrial production is inevitably affecting the environment by emitting harmful and persistent substances, named recalcitrant organic pollutants (ROPs), in the ecosystem. These include agrochemicals, phenols, dyes, surfactants and pharmaceuticals, which persist in soil and water adversely affecting animals' and humans' health [1]. Among pharmaceuticals, antibiotics stand out for the potential development of tolerance between bacterial species, more specifically because of the transfer of a large range of antibiotic resistance genes including those causing diseases [2]. Those strains mutate in the so-called "superbugs", i.e. multidrug-resistant forms characterized by enhanced virulence [3]. Furthermore, ROPs are ineffectively removed in typical wastewater treatment plants [4], which are designed for the purification of aqueous media from a wide range of pollutants including suspended and colloidal particulates as well as dissolved organic matter through physical and chemical treatments. In this context, chemical advanced oxidation processes (AOPs), which degrade these pollutants through oxidation reactions, represent a valid and promising alternative to the current treatments. Indeed, AOPs are characterized by the presence of reactive oxygen species that possess one or more unpaired electrons, the most common being the hydroxyl radical ($^{\bullet}OH$), the superoxide anion radical ($O_2^{\bullet-}$), the hydroperoxyl radical ($HO_2^{\bullet}$) or the alkoxyl radical ($RO^{\bullet}$) [5]. To this end, TiO_2 plays a key role in catalysing the photodegradation of persistent pollutants in wastewater due to its high photostability, non-toxicity, inexpensiveness, photo-reactivity and

* Corresponding author.
E-mail address: matteo.gigli@unive.it (M. Gigli).

https://doi.org/10.1016/j.jwpe.2025.107003
Received 12 September 2024; Received in revised form 6 December 2024; Accepted 12 January 2025
Available online 21 January 2025

chemical and biologically inertness [5]. Upon irradiation, TiO_2 generates electron/hole (e^-/h^+) pairs, in which the holes exhibit a highly positive potential of +2.53 V vs the Standard Hydrogen Electrode [6]. This highly positive potential widens the possibilities towards the photodegradation of organic molecules, as explained by Wu et al. [7], posing valid means against the threat of emerging pollutants. Another peculiarity of TiO_2 lies in its wide bandgap (3.0 eV for rutile, 3.2 eV for anatase and brookite) that allows photoelectrons to yield superoxide anions, widening its application range [8]. These unique properties led to the synthesis of different polymorphs of titania photocatalysts, both as nano- (in the form of spheres, tubes, fibers and sheets) and macrostructures [8]. Different photocatalytic properties were also achieved via the modulation of particle size, specific surface area, pore structure and crystalline phase [8]. For instance, Zhu et al. [9] achieved successful photocatalytic degradation of tetracyclines (TCs), a widely used class of antibiotics, through the application of TiO_2 (P25) nanoparticles in aqueous solution under UV irradiation, reaching >95 % removal within 40 min.

TiO_2 immobilization inside an easily recoverable system makes this semiconductor even more attractive, as this strategy addresses some drawbacks such as poor adsorption, and difficult recovery, separation and agglomeration, all limiting its photocatalytic efficiency [10]. SiO_2-TiO_2 based materials were thus synthetized as core-shell microparticles [11], monodisperse yolk–shell microspheres [12], bi-layer films [13] depending on the targeted application. [14–18]There are several studies where SiO_2 was employed as stable mesoporous support for immobilizing photoactive TiO_2 species, producing TiO_2-SiO_2 mixed oxides. These systems present enhanced photocatalytic activity due to a better dispersion of TiO_2 and increased pollutants adsorption caused by their activation by Ti-O-Si bond [19]. For instance, Jaseela et al. [20] compared the photodegradation activity under visible light of Bisphenol A using both mesoporous TiO_2 and TiO_2-SiO_2 nanocomposites. After 32 min the bare titania achieved only 37 % degradation, while the TiO_2-SiO_2 composite reached 99 %. Conversely, Marques et al. [14,15] studied the fine-tuning of porous hybrid and inorganic silica spherical particles with tailored interconnected macroporosity (MICROSCAFS®) through an adapted sol-gel method combined with polymerization-induced phase separation, assisted by temperatures below 100 °C. These microspheres were subsequently loaded with TiO_2 nanoparticles and employed in continuous flow solar-driven water purification processes [16]. More recent work regarded the implementation of titanium and hafnium precursors directly in the sol-gel synthesis, obtaining a multicomponent oxide SiO_2-TiO_2 and SiO_2-TiO_2-HfO_2 material with interconnected macro- and meso-porosity, expanding the composition range of MICROSCAFS® [17,18].

In line with the need for developing eco-innovative materials aligning with the principles of circular bioeconomy [21], the utilization of biomass waste-derived starting materials is of great interest. They are easily available, cheap and often non-toxic compared to synthetic precursors [22]. Furthermore, their structure possesses internal porosities that favours the entrapment of complex molecules like dyes and antibiotics [23]. Within these materials, chitin, especially in its deacetylated form, i.e. chitosan (CS), holds significant potential. [23]A recent study proposed by Rostami et al. [24] described the synthesis of a stable and biodegradable ternary composite constituted by CS, TiO_2 and multi-walled carbon nanotubes for the adsorption of organic dyes (methylene blue and methyl orange) and of the antibiotic ciprofloxacin in aqueous medium. This composite material showed remarkably high values of maximum adsorption capacity towards all the target molecules, respectively 531.91, 1763.6 and 1510.5 $mg \bullet g^{-1}$, and exhibited stable performances in recyclability tests up to 8 cycles.

Other studies focus on the valorization of fruit shells due to their content of cellulose, hemicellulose and lignin, which inherently contain a high concentration of functional groups [22]. For instance, Buhani et al. [25] proposed a novel system for water remediation by valorizing the carbonaceous material deriving from rubber fruit shells through modification with a silane agent, 3-Aminopropyl Triethoxysilane (APTES), which enhanced the overall adsorption capacity of the system. This bio-based adsorbent demonstrated significant activity in the removal of two differently charged dyes, coomassie brilliant blue (anionic) and methylene blue (cationic) even after a three-cycle reusability test, as an adsorption percentage exceeding 80 % was maintained [25]. In another study Buhani et al. [26] focused on the upcycling of rubber fruit shells, exploring the improvement on their adsorbing activity by conferring magnetic properties to the biomass-derived activated carbon. The adsorption ability towards both organic and inorganic pollutants was further enhanced through subsequent silanization with triethoxy(phenyl)silane. Also in this case, high maximum adsorption capacity of both methylene blue and crystal violet, respectively of 85.060 and 90.504 $mg \bullet g^{-1}$, and high removal percentages exceeding 80 % up to 4 recycles were demonstrated.

In continuity with the above-illustrated research, the present study focuses on the upcycling of rice husk (RH) – a widely available silica-rich biomass residue – as silica source for MICROSCAFS® through the replacement of the expensive and fossil-derived commonly used Si alkoxide tetraethyl orthosilicate (TEOS). The extraction of silica from RH plays a pivotal role in the valorisation of abundant economic waste, which would be otherwise burned contributing to the increase of greenhouse gases emissions [27]. Rice husk abundance is correlated with the high consumption of rice, which represents the staple food for over half of the global population [28]. The product resulting from the RH treatment and calcination is known as Rice Husk Ashes (RHA), a light and highly porous material mainly constituted by SiO_2 (95–98 %) together with potassium, phosphorous and traces of sodium, calcium, magnesium, iron, copper, manganese and zinc in varying percentages depending on geographical factors and harvest year [29]. Silicon is indeed introduced in rice plants via root absorption of its soluble species (silicates or mono-silicic acid), which undergo biomineralization to create a network of lignocellulose and silica [30]. Silica from RH has been employed for several scopes such as water purification, heavy metals adsorption, catalysts preparation, synthesis of composites for construction materials, and biofertilizers production [30]. In terms of bioremediation purposes, Chen et al. [31] investigated the feasibility of RHA application for TCs adsorption from aqueous media, reaching a removal efficiency of 61 % starting from an initial concentration of 5 mg/L. In another study, Costa et al. [32] reported the synthesis of mesoporous silica MCM-41 using silica extracted from RH as an alternative to TEOS. The obtained material exhibited high surface area and the conventional hexagonal mesostructure of the family of ordered mesoporous silicas (M41S), exhibiting high removal percentages in the adsorption of polycyclic aromatic hydrocarbons [32]. Additional evidence supporting its applicability in the framework of water remediation was reported by Niculescu and Raboaca [33], who described the photocatalytic oxidation of the dye Rhodamine 110 under natural light using biobased MCM-41 as catalyst support, and by Alhadhrami et al. [34], who reported the dual activity of SiO_2 nanoparticles synthesized from RHA in both photodegradation of methyl orange under UV irradiation and in the growth inhibition of coliform bacteria in canal water samples.

Building on this ground, the biobased MICROSCAFS® here developed were tested as multifunctional composite materials for water purification, and more specifically for the solar-driven degradation of minocycline (Fig. S1A), a second-generation semi-synthetic tetracycline. It has an expanding broad scope of applications, from safer and efficacious treatment of papulopustular rosacea in the form of topical gel, to the treatment of cancer [35,36]. Tetracyclines contamination in European aquatic environments was recently reported as high as 600–1290 $ng \cdot L^{-1}$ [37,38]. Therefore, their removal from wastewater is attracting increasing interest and, for example, the photocatalytic degradation of minocycline was previously explored with various semiconductor catalysts [39,40]. The physicochemical properties of the RHA-containing MICROSCAFS®, along with the adsorption mechanisms involved and

the photocatalytic activity, are here compared throughout the study with the pristine reference material, i.e. TEOS-based MICROSCAFS®, to highlight any differences and potential advantages deriving from the addition of silica extracted from RH to the system.

2. Experimental section

2.1. Materials

Rice husk (RH) was kindly provided by Riseria delle Abbadesse, located in Grumolo delle Abbadesse, Vicenza, Italy.

Hydrochloric acid (HCl 37 %) and tetraethyl orthosilicate (TEOS 98 %) were purchased by Sigma-Aldrich, (3-glycidyloxypropyl)trimethoxysilane (GPTMS, Xiameter OFS-6040, >98.5 %) was kindly supplied by Dow, and ammonia aqueous solution (25 %) was purchased by Chem-Lab. Decahydronaphthalene (decalin, mixture of *cis* and *trans* isomers, 98 %) and sorbitan monooleate surfactant (Span® 80, HLB: 4.3) were supplied by Merck, titanium isopropoxide (TiPOT 98 %) by Acros Organics and glacial acetic acid (≥99 %) by Fisher Chemical. Minocycline was provided by Hovione S.A. Deionized water was used for all the experiments unless otherwise stated.

2.2. Silica extraction

RH was ground to a 3 mm mesh and boiled under reflux in a 4 M hydrochloric acid solution under magnetic stirring for 2 h. Afterwards, the solid was filtered and washed with water to reach neutral pH. The treated RH was then dried at 90 °C overnight and calcinated in a muffle furnace at 550 °C for 4 h, with a heating rate of 5 °C·min^{-1}. The resulting product, finally ground in a ball mill at 650 rpm for 20 min to obtain a more homogeneous particle size distribution, is hereinafter named RHA.

2.3. Synthesis of rice husk ashes-based MICROSCAFS®

Conventional MICROSCAFS® (MS) synthesis was conducted following the procedure described by Vale et al. [17] with minor modifications. RHA-based MICROSCAFS® (MSR) were prepared by replacing TEOS by specific amounts (20 wt%, 50 wt%, 80 wt% and 100 wt%) of RHA. In detail, after 45 min from the beginning of TEOS and GPTMS pre-hydrolysis, RHA was added to the silanes mixture in the above-reported concentrations. The biobased MICROSCAFS® are named as follows: MSR20, MSR50, MSR80 and MSR100, where the number represents the RHA wt%. Additionally, each sample was calcinated at 900 °C for 30 min. The samples subjected to this heat treatment are identified with the abbreviation "ht". Lastly, a MICROSCAFS® sample containing only GPTMS (MSG) was prepared for sake of comparison, according to the above-described procedure.

A brief techno-economic feasibility of the method adopted for the synthesis of the MICROSCAFS® is reported in SI.

2.4. Characterization

Elemental analysis was carried out on RH, treated rice husk and RHA to determine the content (wt%) of C, H, N and S in each sample. The test was carried out in duplicate by means of a UNICUBE® trace analyzer (Elementar, Lomazzo, Italy), using the method "plant" and sulfanilamide as standard. Prior to the analysis, the samples were dried in vacuum at 40 °C for 24 h.

ICP-OES (PerkinElmer Optima 5300 DV instrument, Waltham, MA, USA) was performed on pristine biomass and RHA to determine the SiO_2 content and on the microspheres to quantify the amount of TiO_2. The procedure for RH and RHA consisted in dissolving 10 mg of sample in 4 mL of HNO_3, 2 mL of H_2O and 0.5 mL of HF (ultrapure for analysis) inside a Teflon container, which was then sealed and put in a microwave digester (Ethos UP Milestone, Bergamo, Italy). Each sample was digested in duplicate using the "dry plant" method and analyzed separately. Lastly, the samples were first diluted to 50 mL and subsequently ten times further prior to the analysis. Silicon was quantified by means of a calibration curve built in the range 0.5–10 mg·L^{-1}.

As to the microspheres, 100 mg of each sample were dissolved in a 2 mL HNO_3 and 5 mL HF mixture and treated in a Ethos UP microwave digester. Each sample was digested in duplicate using the "silica" method and analyzed separately. Afterwards, the samples were first diluted to 50 mL and subsequently 20 times prior to the analysis. Ti was quantified via a calibration curve built in the range 0.5–20 ppm at the wavelength of 337.279 nm.

The chemical structure of RHA and of the prepared MICROSCAFS® was evaluated by Fourier transform infrared spectroscopy in attenuated total reflectance mode (ATR-FTIR) on a PerkinElmer Spectrum Two spectrophotometer (Waltham, MA, USA) equipped with a UATR Two accessory. The following parameters were used for the analysis: spectral range 4000–400 cm^{-1}, 4 cm^{-1} resolution and 8 scans of data accumulation.

X-ray powder diffraction patterns were recorded with conventional Bragg-Brentano geometry at 295 K, with a step size of 0.05° on a scale of 5–145° 2θ and a time of 500 s/step. An Empyrean diffractometer (Malvern Panalytical Ltd.) equipped with Bragg-Brentano HD incident optics, 1/8° divergence slit and copper X-ray tube (wavelength Kα 1.5406 Å) at 40 kV and 40 mA was used. A hybrid 2D solid-state pixel detector PIXcel3D (255 active channels) was employed.

The quantitative phase analysis by X-ray diffraction was performed using the Rietveld method modified by Riello et al. [41]. This method allows to perform the quantitative analysis of the crystalline phases even if an amorphous matrix is present, without adding any internal standards to the sample. The quantification of the different phases, already successfully applied to various materials, particularly to study the crystallization of LAS glass ceramic, [42] is possible because during the crystallization process the whole chemical composition of the sample does not change [42]. The crystallite size distribution was obtained by the Fourier analysis of the fitted peak shape of the anatase corrected for the instrument broadening (Warren-Averbach method) [43].

Thermal stability was determined by thermogravimetric analysis (TGA) using a Hitachi STA7200 thermal analyzer (Ibaraki, Japan). About 5 mg of sample were transferred to an alumina crucible and heated from 35 to 900 °C with a heating ramp of 10 °C·min^{-1} under N_2 flux (200 mL·min^{-1}).

Solid state NMR spectra were recorded at room temperature in a Bruker AVANCE III 500 spectrometer (Bruker, Billerica, MA, USA), operating at B_0 field of 11.7 T, with ^{1}H and ^{29}Si Larmor frequencies of 500.1 and 99.4 MHz, respectively, to gain insight on silicon coordination. All experiments were performed in a 4 mm double-resonance MAS probe (Bruker, Billerica, MA, USA) at 296 K. The samples were sealed into a ZrO_2 rotor with Kel-F caps and spinned at 5 kHz. The spectra were externally referenced to trimethylsilane (^{1}H, 0 ppm) and tetrakis(trimethylsilyl)silane (^{29}Si, −9.9 ppm for $SiMe_3$ group). The ^{29}Si MAS spectra were acquired using the direct observation of ^{29}Si using high power proton decoupling. During the acquisition, a tppm15 decoupling scheme was employed.

Scanning electron microscopy (SEM) images and EDS data were acquired using a Phenom ProX G6 benchtop SEM (ThermoScientific, Waltham, MA, USA). A 15 nm layer of gold was sputtered on the samples before the analysis using a turbomolecular pumped coater Q 150 T ES (Quorum Technologies, Lewes, UK). The size distribution of the microspheres was determined from SEM photographs at 105× magnification by measuring with the ImageJ software the diameter of at least 100 microspheres per sample.

Laser diffraction analysis (LDA) was used to further investigate the size of the MICROSCAFS® in aqueous dispersion. A Mastersizer 3000 (Malvern Panalytical, Malvern, UK), equipped with a Hydro EV wet dispersion unit and an in-line sonication probe for agglomerate dispersion was employed for the test. The microspheres were suspended in water at room temperature and each sample was analyzed eight times.

N_2 adsorption/desorption isotherms were performed on the microspheres at N_2 condensation temperature (77 K) using a Micromeritics Tristar II Plus instrument (Norcross, GA, USA). Before the analysis, each sample was outgassed at 200 °C for 2 h under high vacuum (10^{-3} Torr) to remove moisture and other surface contaminants. The surface area was determined using the Brunauer–Emmett–Teller (BET) method and the average diameter of the pores was calculated using the Barrett-Joyner-Halenda (BJH) method.

Finely crushed MICROSCAFS® were also analyzed using a JASCO UV–Vis spectrophotometer (Easton, MD, USA) equipped with an integrating sphere in the range 190–900 nm to estimate the band gap energy (eV) via the Tauc plot method. It assumes that the energy-dependent absorption coefficient α can be expressed as (Eq. (1)):

$$(\alpha\, h\nu)^{\frac{1}{\gamma}} = B\,(h\nu - E_g) \tag{1}$$

where h is the Planck constant, ν is the photon's frequency, E_g is the band gap energy and B is a constant. The γ factor depends on the nature of the electron transition and for the materials under investigation is equal to 2 (indirect allowed transition band gaps semiconductors). To apply this method, the obtained reflectance spectra were transformed in the corresponding absorption spectra applying the Kubelka−Munk function (Eq. (2)):

$$F(R_\infty) = \frac{(1 - R_\infty)^2}{2\,R_\infty} \tag{2}$$

where R_∞ is the reflectance of an infinitely thick specimen $\left(R_\infty = \frac{R_{sample}}{R_{standard}}\right)$.

Lastly, by substituting $F(R_\infty)$ to α in Eq. (2), the following equation is obtained (Eq. (3)):

$$(F(R_\infty)h\nu)^{\frac{1}{\gamma}} = B(h\nu - E_g) \tag{3}$$

2.5. Adsorption tests

Adsorption tests were performed in dark conditions to determine the maximum adsorption capacity of the prepared MICROSCAFS®. In detail, the samples were mixed with different minocycline solutions (20, 50, 100, 200 and 400 mg·L^{-1}) at the fixed concentration of 1 g·L^{-1} and stirred at 100 rpm and 24 °C for 24 h to reach adsorption-desorption equilibrium. Afterwards, the dispersion was centrifuged at 9000*g* for 10 min and the supernatant was transferred to quartz cuvettes (optical path length 1 cm) and analyzed by means of a JASCO V750 UV–Vis spectrophotometer to determine the absorbance and subsequently calculate the equilibrium concentration through the Lambert-Beer eq. A 4-point calibration curve was built in the range 10–80 mg·L^{-1}, registering the absorbance at 346 nm, the slope of the line being the molar absorption coefficient of minocycline (12,000 mol^{-1}•L•cm^{-1}). A blank sample was prepared by dispersing each MICROSCAFS® in ultrapure water in the absence of minocycline and treating it as the tested samples. Blank samples were then used as reference in the UV–Vis measurements to compensate any possible scattering due to the presence of solid residues that could not be separated by centrifugation.

The adsorption capacity at equilibrium (q_{eq}, mg·g^{-1}), determined as the amount of minocycline adsorbed on the microspheres after 24 h, was calculated as follows (Eq. (4)):

$$q_{eq} = \frac{(C_0 - C_{eq})}{m}\, V \tag{4}$$

where V is the volume of the minocycline solution (10 mL), C_0 is the concentration of minocycline at the beginning of each experiment, C_{eq} is the supernatant concentration measured after 24 h and m is the mass of MICROSCAFS® (0.010 g). Subsequently, Langmuir and Freundlich adsorption models were applied to the acquired data to evaluate the adsorption mechanism of the different samples and their adsorption capacity. The Langmuir model (Eq. (5)) postulates that adsorption takes place as a monolayer on the adsorbent's surface, which has uniform sites with no mutual interactions between adsorbates. This implies that every binding site exhibits identical affinity for the adsorptive:

$$q_{eq} = \frac{q_{max} K_L C_{eq}}{1 + K_L C_{eq}} \tag{5}$$

where q_{max} is the maximum adsorption capacity (mg·g^{-1}), K_L is Langmuir adsorption equilibrium constant (L·g^{-1}) and C_{eq} is minocycline concentration in the supernatant at equilibrium [44]. By contrast, the Freundlich model (Eq. (6)) is an empirical equation that refers to heterogeneous surface energy systems with exponentially decaying adsorption:

$$q_{eq} = K_F\, C_{eq}^{\frac{1}{n}} \tag{6}$$

where C_{eq} is minocycline concentration at equilibrium, K_F [(mg$^{1-1/n}$·L$^{1/n}$·g^{-1})] is the Freundlich adsorption equilibrium constant and n express the favourability of the adsorption process (the higher the value of n, the higher the adsorption capacity at low adsorptive concentration) [45].

The kinetic analysis of minocycline adsorption (10 mg·L^{-1}) was performed using a pseudo-first-order model, described by the following equation (Eq. (7)):

$$ln\frac{C_t}{C_0} = -k\,t \tag{7}$$

where C_t and C_0 are the concentrations at a specific time t and at the beginning of the adsorption experiment (mg·L^{-1}), respectively, k is the adsorption rate constant (min^{-1}) and t is time (min).

2.6. Photocatalytic tests

The photocatalytic activity of the MICROSCAFS® towards the degradation of minocycline was investigated using a solar simulator (model 94011A-ES from Newport, Irvine, CA, USA) equipped with a 100 W Xenon lamp with a standard AM 1.5 G filter. The lamp's technical specifications and its spectral output are reported elsewhere as declared by the producer [46]. The minocycline solution was placed in a thermostated double-jacketed batch reactor. Before each test, the distance between the lamp and the liquid's surface was adjusted, with the aid of a reference cell, to achieve the intensity of 1 sun (1000 W·m^{-2}).

For each experiment, 50 mL of a 10 mg·L^{-1} minocycline solution kept at 19 °C were employed and 50 mg of MICROSCAFS® were dispersed in the solution and mixed at 300 rpm with a magnetic stirrer. The tests consisted of an initial dark period, during which the reactor is not illuminated and covered with aluminum foil, followed by an irradiation period where the solar lamp is on. The initial dark step has a variable duration, as it depends on the adsorption capacity of the tested microspheres.

Every 15 min an 800 μL aliquot was sampled and centrifuged at 7000*g* for 15 min to remove residual fragments of the microspheres. Subsequently, the absorbance of minocycline in the supernatant was determined at λ = 346 nm using a JASCO V-750 UV–Vis spectrophotometer (JASCO, USA) and the corresponding concentration was derived from a calibration curve built in the range 0–40 mg·L^{-1}. A 6-point calibration curve was built in the range 0–40 mg·L^{-1}, the slope of the line being the molar absorption coefficient of minocycline (12,000 mol^{-1}•L•cm^{-1}).

A zero-order kinetic model, defined by the following formula (Eq. (8)), meaning that the rate determining step is the photodegradation reaction, was used to fit the experimental data:

$$C_t = -k\,t + C_0 \tag{8}$$

where C_t and C_0 are the concentrations at a specific time t and at the

beginning of the irradiation phase ($mg{\cdot}L^{-1}$), respectively, k is the photodegradation rate constant ($mg{\cdot}L^{-1}{\cdot}min^{-1}$) and t is time (min).

The degree of degradation was calculated as follows (Eq. (9)):

$$Degradation\% = \left[1 - \frac{C_t}{C_0}\right] \times 100 \quad (9)$$

2.7. Recyclability tests

The recyclability of the best performing MICROSCAFS® sample was evaluated by a 4-cycle test. At the end of each photodegradation cycle, a 1 mL aliquot was collected and analyzed to calculate the concentration of minocycline. Based on the determined value, the amount of minocycline needed to restore the initial concentration (10 $mg{\cdot}L^{-1}$) and 1 mL of H_2O to restore the initial volume (50 mL) were added to the reactor at the beginning of each subsequent cycle.

2.8. LC-HRMS analysis

The supernatant sampled at the end of each photocatalytic test was analyzed by means of liquid chromatography quadrupole time-of-flight mass spectrometer (LC/Q-TOF MS, Bruker, Billerica, MA, USA) to determine the residual concentration of minocycline and the presence of possible by-products formed during exposure to solar light. The minocycline content was quantified through a 5-point calibration curve, which ranged from 0.30 to 5 $mg{\cdot}L^{-1}$. The chromatographic run was performed on a BEH C18 column 130 Å (75 × 2.1 mm, 2.5 μm particle size) (Waters, Milford, MA, USA) at 50 °C, using a flow rate of 0.3 $mg{\cdot}min^{-1}$. The mobile phase was 0.1 % of formic acid in water (eluent A) and in methanol (eluent B), using an optimized elution gradient. The mass spectrometer operated in positive/negative mode, with a capillary voltage of 2500 V (+)/3500 (−), a nebulizer pressure of 3 bar, dry temperature of 250 °C and 9 $L{\cdot}min^{-1}$ as dry gas flow. The acquisition was performed in Auto MS/MS mode selecting a mass range of 30–1000 Da.

3. Results and discussion

The calcination at 550 °C of the acid-treated rice husk yielded 16 wt % SiO_2, in full agreement with literature data [47]. As determined by elemental analysis, the content of C, H, N and S in RHA was respectively equal to 0, 0.9 ± 0.1, 0 and 0.23 ± 0.03 wt%, demonstrating, differently from RH, the absence of carbonaceous matter (Table S1). Furthermore, ICP-OES analysis showed that 92 % of the obtained fine white powder is constituted of SiO_2 (Table 1), indicating that RHA consists mostly of silica, while small percentages of metal oxides like CaO, MgO, K_2O might be present [48]. This result is further supported by FT-IR analysis (Fig. S2A), whose spectrum is characterized by the silanes' typical vibration modes such as asymmetric and symmetric stretching of Si-O-Si group at ca. 1100 and 800 cm^{-1}, a weak band at 470 cm^{-1} attributable to its bending mode vibration, and the broad band at 3450 cm^{-1} relative to the -OH stretching vibration of silanol groups and of residual sample humidity [49,50]. Lastly, the C—H stretching bands present in the range 2800–3000 cm^{-1} can be ascribed to the adsorption of contaminants from the environment, as carbon was not detected in the sample by CHNS measurements. RHA diffractogram (Fig. S2B) is characterized by a wide diffused peak centred at $2\theta = 22°$, distinctive of amorphous SiO_2 [51], and its thermogravimetric curve (Fig. S2C) revealed stability up to 900 °C, in agreement with literature data [29].

Table 1
Silicon content expressed in mg g^{-1} obtained from ICP-OES analysis conducted on rice husk (RH) and rice husk ashes (RHA).

Sample	Si (mg g^{-1})	SiO_2 (%)
RH	124 ± 1	26 %
RHA	429 ± 10	92 %

With the main purpose of determining the nature of the Si species constituting the prepared microspheres, ^{29}Si MAS-NMR spectroscopy was carried out on RHA, MSR100 and MSG (Fig. 1). These samples were chosen to verify whether the Si units present in RHA and in MSG, where the peaks are ascribable only to the Si derived from GPTMS, were both visible in MSR100, to thus confirm the incorporation of RHA in the MICROSCAFS®. The conventional notation Q^n and T^m, which respectively stand for tetrafunctional and trifunctional Si centres, was used to describe the units [52]. Specifically, Q refers to $[(SiO)_n\ Si\ (OH)_{4-n}]$ units, where n is the number of bridging oxygen atoms surrounding the central silicon atom, whereas T indicates $[(SiO)_m\ RSi\ (OH)_{3-m}]$ units, where R symbolizes the 3-glycidyloxypropyl group connected to the central Si. In the RHA spectrum, three peaks representing three different environments of silicon atoms are visible. At −89 ppm a weak shoulder indicating the presence of Q^2 units, i.e. a silicon atom bonded with two siloxane groups and two silanol groups, is also detected. The most intense peak at −107 ppm (Q^4 units), and a more prominent shoulder at −98 ppm (Q^3 units), respectively represent Si connected to four and three siloxane groups [53]. The amount of the three units is correlated to the relative intensity of their peaks (deconvoluted spectra are shown Fig. S3). In RHA, the most abundant unit is Q^4, suggesting that almost all the network is condensed, apart from a fraction of uncondensed Si-OH groups. On the other hand, in the MSG spectrum T^2 and T^3 peaks of the same intensity, respectively localized at −54.0 and −63.0 ppm, are present. This result indicates that in this case Si is covalently bonded to one alkyl group and to two and three siloxane groups, respectively [52].

Finally, in the case of MSR100, both T and Q units can be observed. Nevertheless, the Q^4/Q^3 ratio is higher for MSR100 than for RHA, suggesting more homocondensation (more siloxane bonds). Thus, RHA and GPTMS reacted to form a siloxane network constituted by both compounds, indicating an effective incorporation of RHA in the MICROSCAFS®.

Subsequently, SEM analysis was carried out to evaluate the surface and bulk structure of the different microspheres and to obtain information about particle size (Fig. 2).

MS (Fig. 2A-B) and MSR20 (Fig. 2C-D) present similar shape and internal porosity, as visible from the enlargement of the inner particles' core. Their morphology agrees with literature data [17]. Contrarily, for TEOS substitution higher than 20 %, the microspheres are bigger and their morphology changes. For example, Fig. 2F shows that nucleation took place inside the spheres rather than polymerization-induced phase separation (spinodal decomposition) which would have led to the formation of the interconnected porous MS structure. By further increasing the degree of TEOS substitution, not only the size of the particles increased, but also their core-shell structure further varied, as a hollow structure with high surface porosity could be observed (Fig. 2J). The bigger dimensions of RHA-rich MICROSCAFS® can be ascribed to the enlargement of the emulsion's water droplets disrupted by the RHA powder. In fact, an in-depth evaluation of the size distribution of the prepared MICROSCAFS® (Fig. S4 and Table S2) confirmed that by increasing the content of RHA the average particle diameter was enhanced. This phenomenon is even more evident for MSR80 (119 ± 67 μm) and MSR100 (115 ± 49 μm), which display an almost doubled size with respect to MS (62 ± 21 μm). On the contrary, the spherical shape and average diameter of MSG did not significantly change compared to MS, further strengthening the hypothesis of an emulsion destabilization process, i.e. emulsion's droplets coalescence, in the presence of RHA. Lastly, MSG microspheres display an empty core as the RHA-containing ones, although a more uniform surface is preserved (Fig. 2L). Hence, it can be concluded that the generation of an interconnected macroporous domain inside the emulsions' water droplets can be achieved up to a TEOS replacement of 20 wt%. This aligns with previous studies, which state that higher GPTMS contents lead to a lower condensation rate compared to tetraalkoxysilanes, this effect being further enhanced by the steric hindrance of the alkyl chain [17].

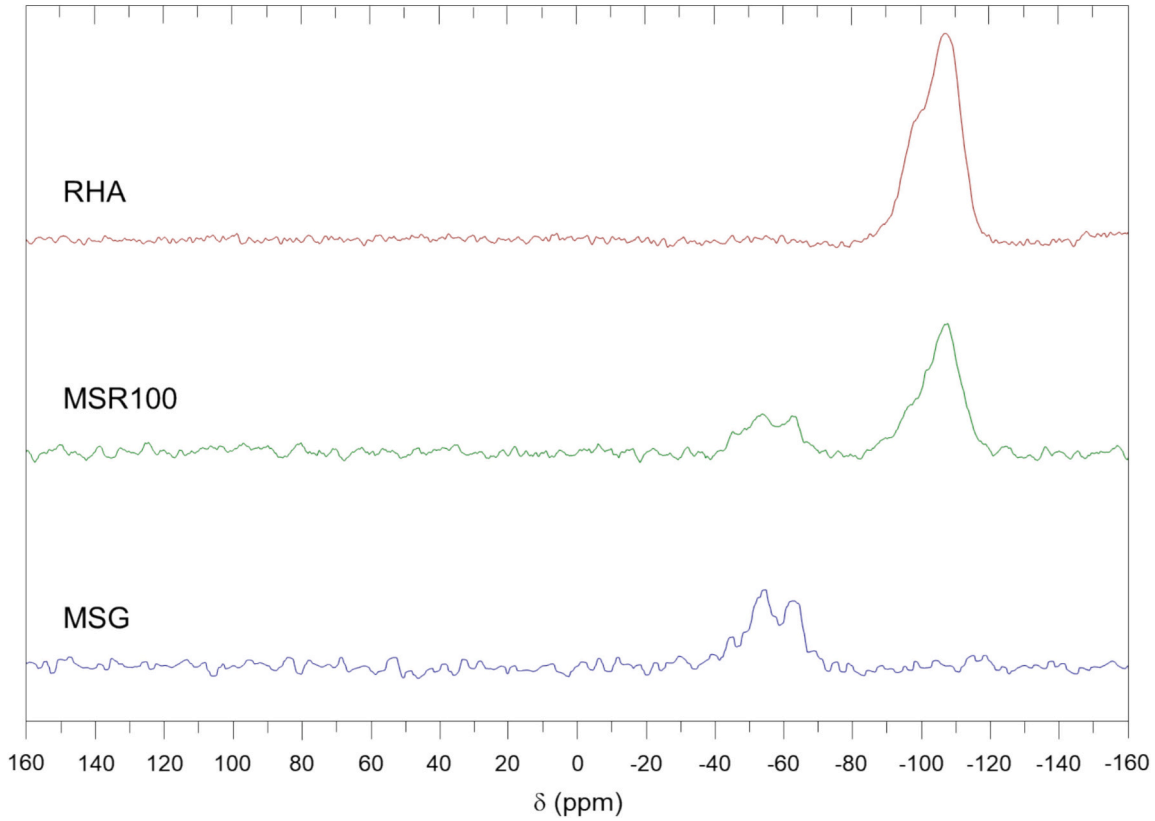

Fig. 1. ^{29}Si MAS spectra of RHA, MSR100 and MSG.

Among all the synthesized MICROSCAFS®, to maximize the valorisation of RH, MSR100 were selected for further analysis, together with MS as reference. Furthermore, to obtain fully inorganic microspheres with increased thermal and chemical stability, a calcination treatment at 900 °C was conducted on these two samples. The weight loss at the end of the calcination process decreased with the increase of the RHA content (53.6 % for MS vs 35.7 % for MSR100), providing further proof of the involvement of RHA in the sol-gel polycondensation reaction with GPTMS. Indeed, the amount of organic moiety is lowered by enhancing the RHA content, and RHA is stable at 900 °C (Fig. S2C).

Structural changes on the MICROSCAFS® induced by the substitution of TEOS with RHA and by the calcination procedure were investigated by FT-IR analysis (Fig. S5). As to MS, a broad band centered at 3400 cm^{-1}, resulting from the ν_{as} (-OH) of silanol groups and physisorbed moisture, could be detected [14]. The weak band at ca. 1250 cm^{-1} corresponds to the epoxide symmetric ring breathing vibration of GPTMS, while the peaks at 2930 cm^{-1} and 2860 cm^{-1} are due to stretching vibrations of -CH_2 groups in decalin, Span80 and GPTMS [14,17]. The presence of traces of the surfactant Span80 is also evident from the bands at 1200 cm^{-1} (ν_{as} C═O), and at 1410 cm^{-1} (δ O—H) [17]. Furthermore, the peak at ca. 1060 cm^{-1} may be ascribed to the asymmetric stretching of Si-O-alkyl groups and Si-O-Si groups derived from polycondensation of the silanes or, in the case of MSR100, of the hydrolyzed RHA with Si-OH from hydrolysed GPTMS. The band at ca. 960 cm^{-1} can be attributed to Si—O asymmetric stretching in Si-O-Ti, and to Si-OH bonds [54,55]. In line with NMR data, its relative intensity is lower for MSR100 than MS, suggesting that MSR100 contains more Q units, while in MS more heterogeneous condensation occurs, therefore more Si-O-Si bonds are present. Lastly, the peak at ca. 440 cm^{-1} reflects the stretching vibrations of Ti—O bond in TiO_2 [56–58], which results from the use of TiPOT.

The FT-IR spectra of heat-treated samples show significant changes, as the materials are fully inorganic systems. All the bands relative to traces of Span80, decalin, water and other organic residues are no longer discernible. Indeed, only the asymmetric stretching of the Si–O–Si homogeneous pattern (at 1040 cm^{-1}), the overlapped bands relative to stretching vibrations of Si—O in Si–O–Ti achieved through heterocondensation (960 cm^{-1}) and the stretching vibration of Ti-O-Ti (440 cm^{-1}) can be observed [56–58].

Finally, the Si-O-Si band peaked at ~1090–1050 cm^{-1} is broader for MSR100ht than for MSht, possibly due to an overlapping of bands ascribed to a variety of Si species, such as T units and Q units, as detected by ^{29}Si MAS-NMR.

In view of their application in aqueous media, the size of the selected samples was also analyzed by LDA and the results are reported in Fig. S6 and Table S3. The average dimensions (Dx 50) of MS and MSR100 are slightly higher than those obtained by SEM analysis, suggesting possible agglomeration phenomena in water. On the opposite, after the calcination, a lower hydrodynamic diameter was observed, indicating a colloidal stabilization effect induced by the heat treatment.

As porosity plays an important role in the adsorption behaviour, the microspheres were subjected to physisorption studies to determine surface area and pores' size. Fig. S7 shows the isotherms of N_2 physisorption for MS, MSR100, MSht and MSR100ht, as well as the distribution of pores obtained through the application of the BJH method. At a first glance, MS (Fig. S7A) seems to display a type III isotherm, which refers to non-porous or macroporous materials. However, with a deeper analysis, a tight H3 hysteresis loop can be identified at high relative pressures, meaning that the sample is also endowed with mesopores (Fig. 2B). Similar considerations can be made for the corresponding heat-treated sample (MSht). which also shows a type III isotherm (Fig. S7C) in agreement with previous data [17]. Furthermore, both MS and MSht display a bimodal pore distribution, with a fraction of mesopores peaked at 5 nm and a broad distribution of macropores ranging from 100 to 140 nm. The surface area is respectively equal to 18.17 m^2 g^{-1} and 14.10 m^2 g^{-1}.

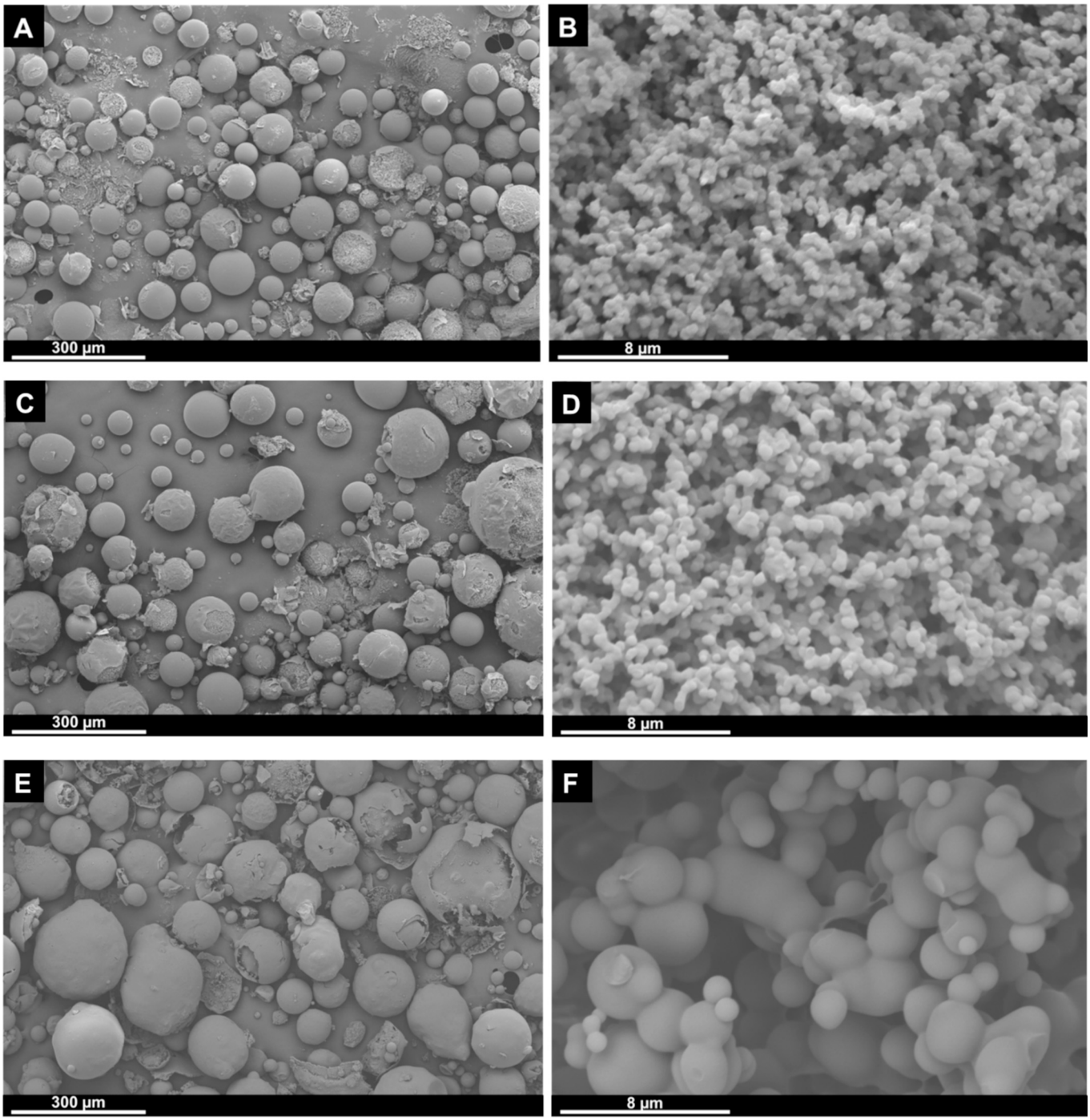

Fig. 2. SEM images of MS (A, B), MSR20 (C, D), MSR50 (E, F), MSR80 (G, H), MSR100 (I, J), and MSG (K, L). Scale bar (A,C,E,G,I,K) = 300 µm; Scale bar (B, D, F, H, J, L) = 30 µm. Each image on the right represents a higher magnification of the respective left side picture.

As to MSR100, the physisorption experiments revealed its non-mesoporous nature and an extremely low surface area value of 1.20 $m^2\ g^{-1}$, rendering the measure unreliable (Fig. S7B). On the contrary, MSR100ht exhibits a type IV isotherm (Fig. S7D) together with a relatively high surface area equal to 91.81 $m^2\ g^{-1}$. The shape of the hysteresis can be identified as H5, suggesting that MSR100ht has a particular pore structure containing both open and partially blocked mesopores [59], whose distribution is centred at 5 nm.

Calcination leads to the loss of organic species, which could act as active sites of adsorption. However, this treatment did not significantly modify the surface of MS, nor its size distribution, while, in the case of MSR100, it led to the promotion of pore formation, drastically increasing the surface area. As RHA showed a slight mass loss (ca. 5 %) upon heating to 900 °C (Fig. S2C), this phenomenon might have contributed to such pore formation.

Since the photoactivity of the samples could be ascribed to the intrinsic presence of TiO_2 (vide infra), ICP-OES and XRD analysis were performed to quantify its content [41]. The results are presented in Table 2, while the XRD diffractograms are reported in Fig. S8.

The calcinated samples displayed higher TiO_2 content due to the removal of organic substances. The increase was more significant for MS than MSR100 due to the higher concentration of organic matter prior to

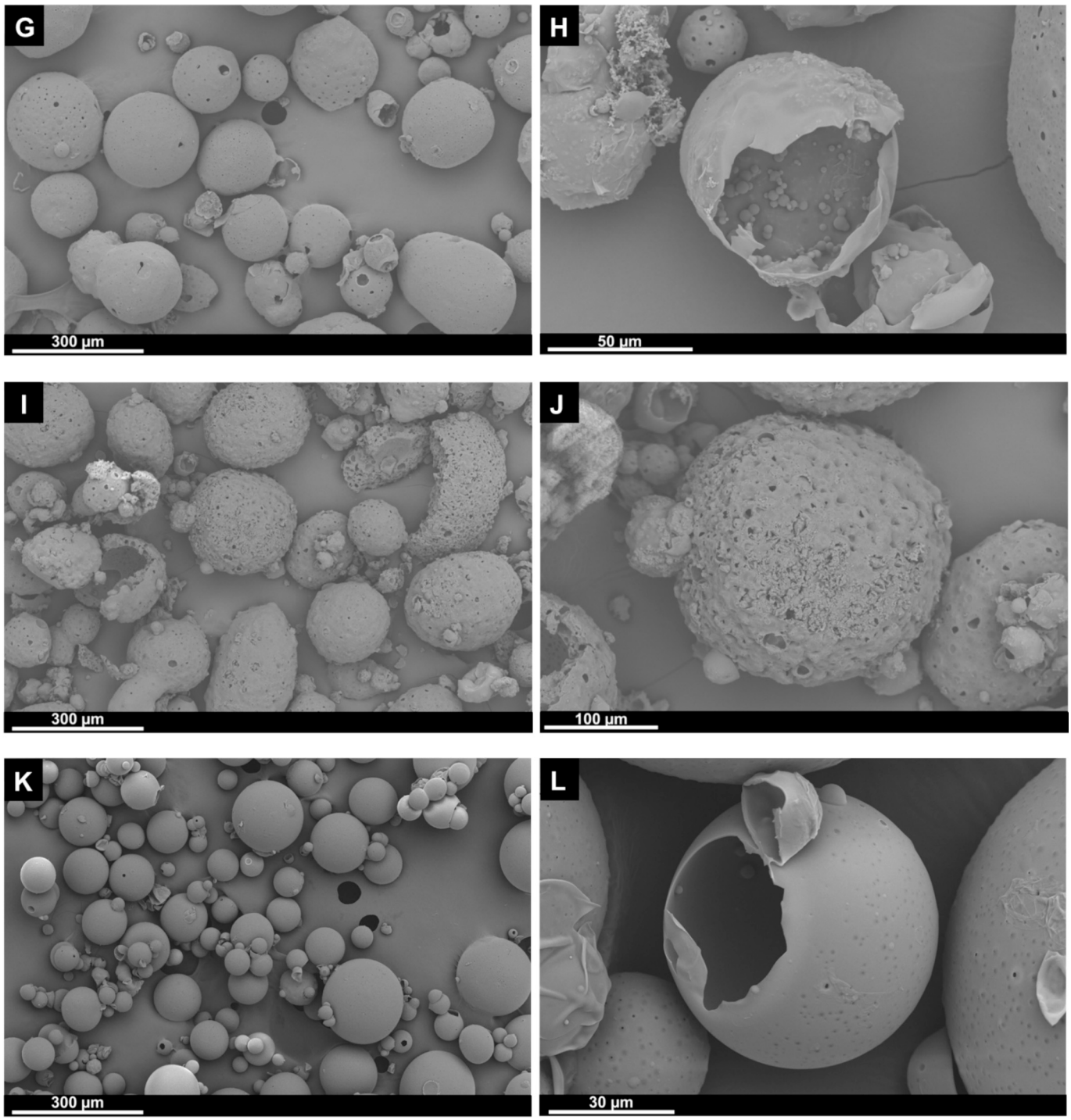

Fig. 2. (*continued*).

Table 2
Specific surface area, TiO_2 content from ICP-OES and XRD, crystallite dimensions and band gap energy values for MS, MSR100, MSht and MSR100ht.

Sample	Surface area (m^2 g^{-1})	TiO_2 content (%) (ICP-OES)	TiO_2 content (%) (XRD, anatase)	Crystallite dimensions (nm)	Band gap energy (eV)
MS	18.17	11.1 ± 0.2	–	–	3.59
MSR100	1.20	8.2 ± 0.1	–	–	3.53
MSht	14.10	23.4 ± 0.7	17 ± 2	1.8	3.27
MSR100ht	91.81	12.7 ± 0.2	10 ± 1	3.4	3.21

the heat treatment. Of note, the amount of Ti contained in MSR100 is lower than that in MS, in agreement with the loading used in the synthesis.

To confirm the higher TiO_2 concentration in MSht, quantitative phase analyses on XRPD pattern were performed. The results show that only anatase (ICSD 9852) was produced during the synthesis. Therefore, quantitative calculations (Fig. 3A-B) were carried out [41,42] and the data are collected in Table 2. [43]

XRD analysis is in full agreement with ICP-OES data, confirming a higher TiO_2 content in the MSht sample with respect to MSR100ht, although the reported values are lower. This result can be ascribed to the

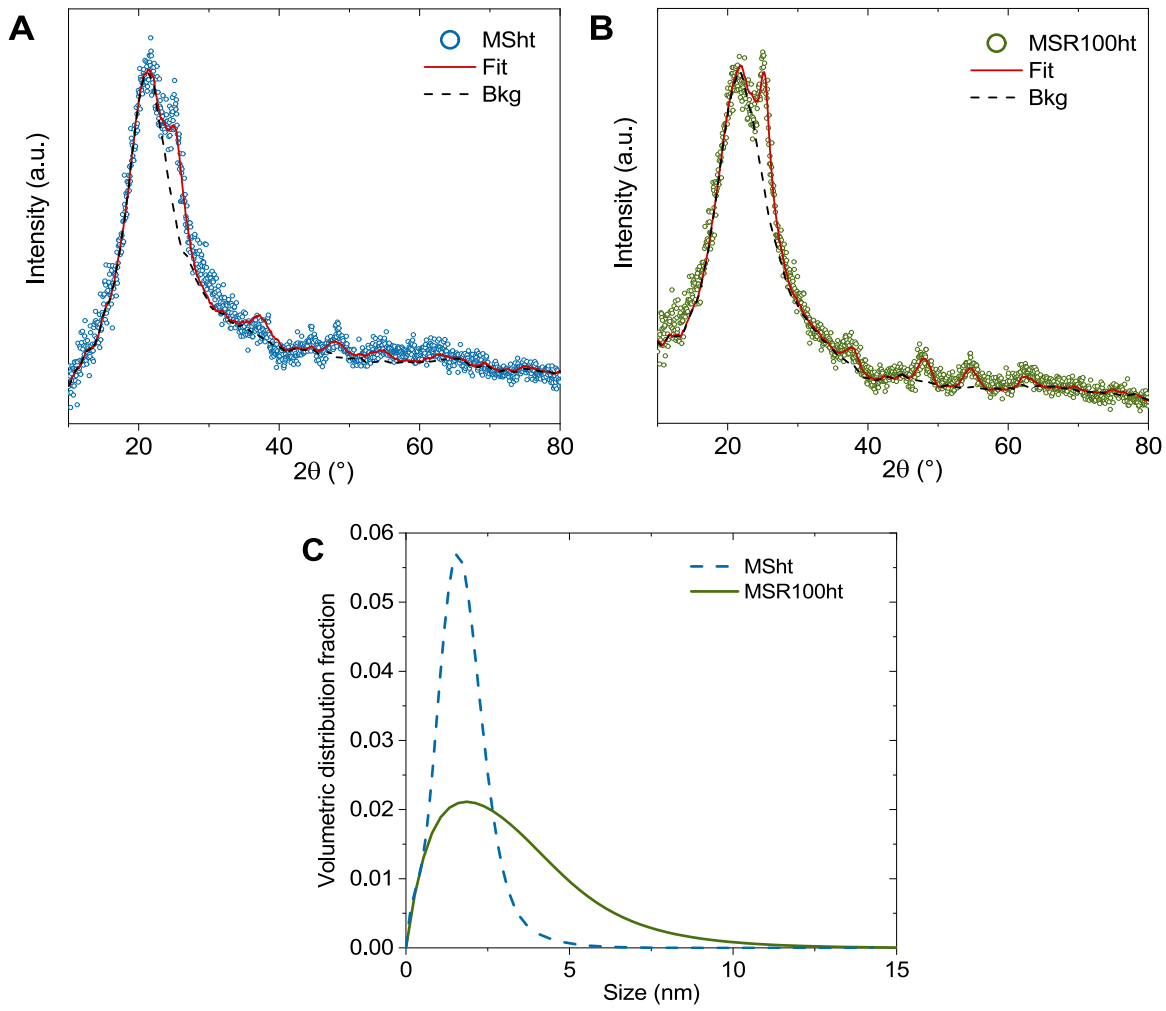

Fig. 3. XRPD and fitted diffraction pattern of MSht (A), MSR100ht (B), and calculated crystallite dimensions (C) for MSht and MSR100ht.

partial diffusion of Ti ions into the SiO_2 amorphous matrix. Additionally, the crystalline phase of MSR100ht presents sharper peaks than MSht, which may be attributed to different crystallite dimensions. To confirm this hypothesis, the crystallite size distribution was calculated with the Warren-Averbach method [43]. As shown in Fig. 3C, the anatase crystallites in MSR100ht are almost double in size than those in MSht, their diameter being respectively equal to 3.4 and 1.8 nm.

The heat treatment also impacted the band gap energy in both MS and MSR100, which respectively decreased after the calcination step from 3.59 eV to 3.27 eV and from 3.53 eV to 3.21 eV. The obtained values resulted larger than the typical band gap energy of TiO_2, which corresponds to 3.2 eV for anatase and 3.0 eV for rutile, probably due to the different chemical environment [60].

The photocatalytic activity of the samples towards minocycline was subsequently studied. First, experiments in dark conditions were performed to reach adsorption-desorption equilibrium and to determine the adsorption capacity. The obtained adsorption isotherms (Fig. S9) were fit using Langmuir and Freundlich models to understand the adsorption mechanism. High correlation coefficients were obtained by applying the Freundlich model for MS ($R^2 = 0.99$) and the heat-treated samples, i.e. MSht ($R^2 = 0.91$) and MSR100ht ($R^2 = 0.94$). In the case of MSR100, the Freundlich model still presented a higher correlation coefficient (0.72) than the Langmuir model (0.51), although the R^2 values were both lower than 0.9, meaning that other mechanisms could be involved in the adsorption process.

According to the Freundlich model, adsorption occurs at energetically heterogeneous sites, with the formation of adsorbate multilayers [61]. Adsorption equilibrium constant (K_F), adsorption intensity (1/n) [62], and the maximum adsorption capacity (q_{max}) determined for a minocycline concentration of 400 $mg{\cdot}L^{-1}$ (the highest tested concentration), are listed in Table 3.

Freundlich's n parameter expresses the mean energy of adsorption, with values higher than 1 suggesting a strong adsorbent/adsorptive interaction and markedly heterogeneous adsorption site energies [63]. On these bases, it can be inferred that all samples showed high affinity with minocycline, with MSR100ht displaying the highest value. These considerations are confirmed by the value of K_F, which represents the adhesion ability of the adsorbate onto the adsorbent (relative adsorption capacity of the adsorbent) [61], that displays the highest value for MSR100ht among the studied samples. This could originate from the relatively high surface area (91.81 $m^2\ g^{-1}$) of this material, which promoted minocycline adsorption.

Table 3
Empirical parameters of Freundlich's equation (K_F, n) and minocycline adsorption capacity (q_{eq}) for MS, MSR100, MSht and MSR100ht (minocycline solution C_0: 20, 50, 100, 200, 400 $mg{\cdot}L^{-1}$; V = 10 mL; T = 25 °C; time: 24 h; stirring speed: 100 rpm; adsorbent mass: 10 mg).

Sample	K_F [$mg^{1-1/n}\ L^{1/n}\ g^{-1}$]	n	q_{max} ($mg\ g^{-1}$)
MS	12.86 ± 2.18	3.06	86.80 ± 9.29
MSR100	7.04 ± 5.43	2.90 ± 1.25	67.18 ± 15.71
MSht	8.14 ± 2.89	3.07 ± 0.65	56.86 ± 7.60
MSR100ht	20.78 ± 4.15	4.38 ± 0.79	80.81 ± 10.05

In this context, it is important to consider the protonation state of minocycline in solution. Indeed, minocycline bears four hydroxyl groups and two dimethylamino groups, which confer a complex charge behaviour as a function of pH. At pH 6.4, i.e. the experimental conditions employed in the present work, minocycline exists in its zwitterionic form (Fig. S1B), exhibiting an absorption maximum at 346 nm [64]. In this state, one dimethylamino group is protonated and one hydroxyl group is deprotonated. Moreover, at this pH, the MICROSCAFS® presented an overall neutral surface charge [65]. The minocycline-particle interaction can thus be ascribed to the formation of hydrogen bonds involving amide, carbonyl and phenolic groups of minocycline and the Si-OH and Ti-OH groups on the surface of the MICROSCAFS® [66].

The kinetic analysis of minocycline adsorption revealed that a pseudo-first-order model could reliably describe the recorded trends for all the samples (Fig. S10), suggesting a diffusion-controlled adsorption process.

On the other hand, the adsorption kinetics (Table 4) evidence that MS exhibited the best performance ($k = 2.2\ 10^{-2}\ min^{-1}$), while the heat treatment caused a reduction of the adsorption rate by an order of magnitude ($2.2\ 10^{-3}\ min^{-1}$). This result could be ascribed to the lower surface area of the heat-treated sample. An opposite trend was observed for MSR100 ($3.1\ 10^{-3}\ min^{-1}$) and MSR100ht ($4.0\ 10^{-3}\ min^{-1}$) as a consequence of the 76-fold increase of surface area induced by the calcination.

After the establishment of adsorption-desorption equilibrium, the samples were irradiated with simulated solar light (1 sun) and the corresponding minocycline photodegradation kinetics were studied (Fig. 4).

In the case of MS (Fig. 4A), due to the rapid adsorption step, the irradiation was started before reaching the adsorption-desorption equilibrium plateau to verify the ability of MS to photodegrade minocycline by observing any slope changes of the kinetic curve. Nevertheless, this did not occur. It is also worth pointing out that a longer test with MS would have been difficult due to the mechanical fragility of the microspheres, as many already broke during the 3 h test. This did not happen for MSR100, which maintained their integrity over a much longer timeframe, implying that RHA increased the overall stability of the system.

The photodegradation kinetics of minocycline could be described using a zero-order kinetic model (Fig. S12), suggesting a surface reaction limited process characterized by a relatively fast adsorption equilibrium and a relatively slow surface reaction. Under these experimental conditions, the surface of the MICROSCAFS® is saturated with minocycline, the rate determining step being the photodegradation reaction [67]. The highest photodegradation rate was obtained using MSR100ht ($k = 7.6 \bullet 10^{-2}\ mg \bullet L^{-1} \bullet min^{-1}$), followed by MSht ($3.7 \bullet 10^{-2}\ mg \bullet L^{-1} \bullet min^{-1}$) and MSR100 ($1.6 \bullet 10^{-2}\ mg \bullet L^{-1} \bullet min^{-1}$) (Fig. S12 and Table 4). This result well correlates with the specific surface area of the samples and with the presence of TiO_2 crystalline phases (Fig. 3). MSR100 exhibited the scarcest performance (45 % degree of degradation in 165 min irradiation) due to the very low specific surface area and to the absence of TiO_2 crystalline phases. Conversely, the relatively high specific surface area of MSR100ht and the presence of larger anatase crystallites allowed to reach a complete removal of minocycline in 45 min. Another factor that influences the photodegradation rate is the energy band gap value (Table 2). In this regard, the narrower the energy band gap, the higher the number of photons absorbed per unit time and area, resulting in an enhanced photocatalytic activity.

Therefore, the substitution of TEOS with RHA endows the particles with superior features for an efficient removal of minocycline from water. In terms of photodegradation mechanism, tetracycline molecules possess a delocalized π system connected with a hydroxyl group (Fig. S1A), which lowers the gap between HOMO and the LUMO to 1.97 eV, making it capable of absorbing visible light [7]. Minocycline can form a surface complex with TiO_2 under visible light irradiation [68], allowing the transfer of the visible-excited photoelectrons from the LUMO of minocycline to the conduction band (CB) of TiO_2 (Fig. 5). Therefore, the electrons in the CB of TiO_2 can be transferred to O_2 forming the radical $\dot{O}_2^-$, capable of degrading minocycline to stable products [7]. Moreover, the concurrent holes' generation in the valence band (VB) of TiO_2 can react with H_2O to produce hydroxyl radicals capable of reacting with minocycline towards the formation of other by-products (vide infra) [69].

LC-HRMS analysis was conducted on the supernatant aliquots sampled during the photocatalytic tests to better quantify the decrease in minocycline concentration and to detect the presence of common degradation by-products. Specifically, TP431 (of proposed empirical formula $C_{21}H_{22}N_2O_8$, Fig. S1C) was the only compound identified. Its presence is attributable to the attack by photogenerated hydroxyl radicals leading to hydrogenation and cleavage of a dimethylamino group of minocycline [69].

The results obtained from LC-HRMS (Fig. 6A) revealed residual minocycline concentration values comparable to those obtained through UV–Vis spectroscopy. In particular, the test conducted on sample MS resulted in a final concentration of 0.49 mg/L, compared to 3.50 mg/L for MSR100. On the other hand, for MSht and MSR100ht the minocycline final concentrations were 0.92 mg/L and 0.15 mg/L, respectively.

The TP431 by-product was found in all four ion chromatograms, with the highest concentration observed for MSht, followed by MSR100ht, MSR100 and MS. The effective conversion of minocycline to TP431 is an important factor, as TP431 is overall non-toxic to fish, green algae and daphnids, unlike the parent antibiotic [69]. In fact, in terms of acute toxicity, minocycline is harmless to fish, but harmful to green algae and toxic to daphnids. Conversely, as for chronic toxicity, it is harmful to fish and toxic to daphnids and green algae. The results presented in this study demonstrate that these noxious effects can be minimized under solar irradiation in the presence of the developed MICROSCAFS®.

Lastly, the recyclability of the best performing sample (MSR100ht) was evaluated over four photodegradation cycles (Fig. 6B). In this case, the experiment was carried out using the same concentration of minocycline and mass of the catalyst of the previous tests, the only difference being a 90-minute solar irradiation. The results show that the MSR100ht performances were overall maintained, meaning that the RHA-based system is not only stable over the degradation of minocycline, but can also be efficiently recovered and reused.

Table 4
Kinetic constants of adsorption (min^{-1}) and photodegradation ($mg \bullet L^{-1} \bullet min^{-1}$) calculated during the tests (minocycline solution C_0: 10 $mg \cdot L^{-1}$; V = 50 mL; T = 19 °C; stirring speed: 300 rpm; adsorbent mass: 50 mg).

Sample	$k_{adsorption}$ (min^{-1})	$k_{photodegradation}$ ($mg \bullet L^{-1} \bullet min^{-1}$)
MS	$2.2\ 10^{-2}$	–
MSR100	$3.1\ 10^{-3}$	$1.6\ 10^{-2}$
MSht	$2.2\ 10^{-3}$	$3.7\ 10^{-2}$
MSR100ht	$4.0\ 10^{-3}$	$7.6\ 10^{-2}$

4. Conclusions

In this study, silica extracted from rice husk (RHA) was for the first time incorporated into MICROSCAFS®. The synthetic process is based on a sol-gel method combined with polymerization-induced phase separation, where RHA replaced the standard TEOS alkoxide in varying amounts ranging from 20 wt% to 100 wt%, in alignment with the principles of circular economy and sustainability. The process is easily scalable, as a preliminary scale-up test using a 2 L oil-jacketed reactor equipped with a turbine-shaped stirrer to produce conventional MICROSCAFS® was successfully carried out. The substitution of TEOS with RHA is not expected to introduce additional complexity or constraints to the scaled-up synthesis, as a homogenizer inducing high shear

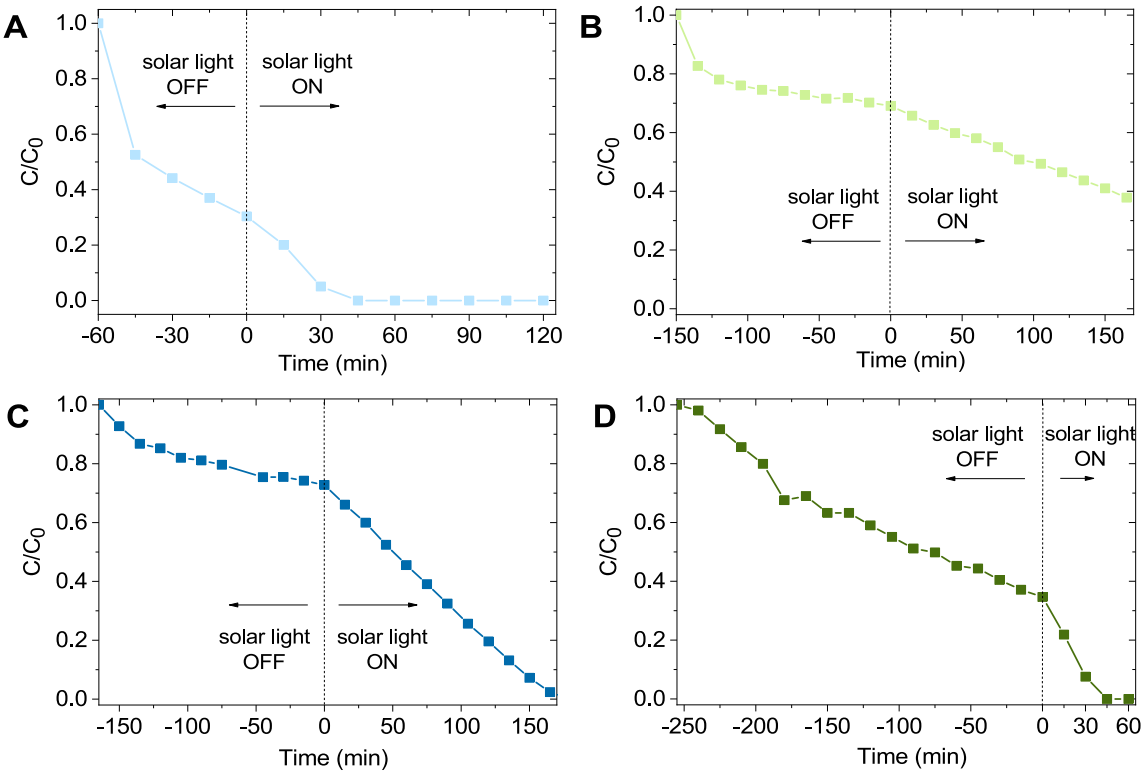

Fig. 4. Temporal variation of C/C_0 of MS (A), MSR100 (B), MSht (C) and MSR100ht (D) recorded during the photocatalytic tests carried out in the following conditions: 50 mg of MICROSCAFS®, initial minocycline concentration of 10 mg•L^{-1}, 1 sun irradiation, 19 °C and 300 rpm. The corresponding UV–Vis absorption spectra are reported in Fig. S11.

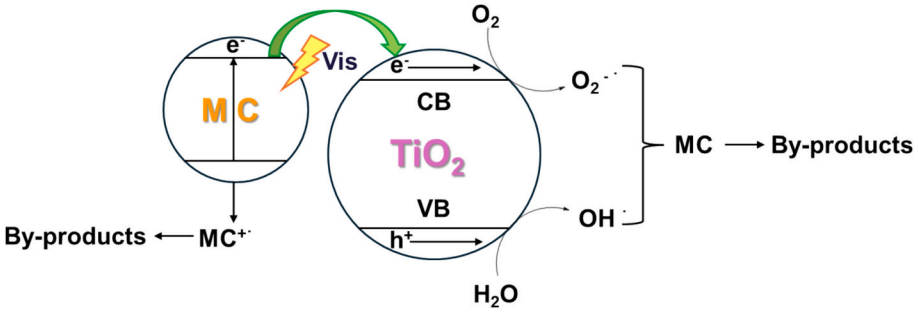

Fig. 5. Possible photocatalytic mechanism of TC degradation by TiO_2 under visible light irradiation [7].

stress is employed in the process. Furthermore, the extraction of silica from RH involves conventional steps of grinding, boiling, filtration/washing, and drying/heat treatment at 550 °C.

Among the synthesized samples, MRS100 and its calcinated form (MSR100ht) were selected for further characterization and testing to maximize the valorisation of RHA, and the results were compared to the conventional MICROSCAFS®. Proof of RHA introduction emerged from several analytical techniques. ^{29}Si MAS-NMR spectroscopy evidenced both RHA and GPTMS silicon coordination sites (Q and T units) in the MSR100 sample, while SEM analysis revealed the morphological differences in size (along with LDA measurements) and internal pore structure between the conventional and the bio-based sample. Additionally, FT-IR spectroscopy showed that MSR100 and MSR100ht display a heterogeneous condensation-related band, at ca. 960 cm^{-1}, yet of lower intensity than that of MS and MSht, and a broader Si-O-Si related band resulting from the variety of Si species (Q and T units), in agreement with the MAS-NMR results.

Physisorption analysis demonstrated that MSR100ht has the highest surface area (91.81 m^2 g^{-1}) and a pore size distribution centered at 5 nm, confirming the primary presence of mesopores as suggested by the type IV isotherm. ICP-OES analysis revealed that the TiO_2 content in MSR100ht is half the value of MSht (12.73 % vs 24.41 %), and XRD analyses evidenced the formation of anatase crystallites in both heat-treated samples, whose size was 3.4 and 1.8 nm, respectively. These data suggest that the presence of RHA might have promoted the formation of larger anatase crystals. As to MS and MSR100, no crystalline phases could be detected as only the broad band of amorphous SiO2 at $2\theta = 22°$ was visible, correlating with their low photocatalytic activity showed during the solar-driven photocatalytic tests. MSR100ht displayed the highest minocycline photodegradation, achieving a complete removal in 45 min, compared to 165 min needed for MSht. Moreover, the kinetic constant of photodegradation of MSR100ht ($7.6•10^{-2}$ mg•L^{-1}•min^{-1}) doubled that of MSht ($3.7•10^{-2}$ mg•L^{-1}•min^{-1}). The high removal efficiency of MSR100ht could be ascribed to the relatively higher specific surface area and crystallinity, and to the relatively lower band gap energy (3.21 eV) with respect to the other materials. LC-HRMS measurements carried out on the aqueous phase after the photodegradation experiments evidenced the presence in all samples of one

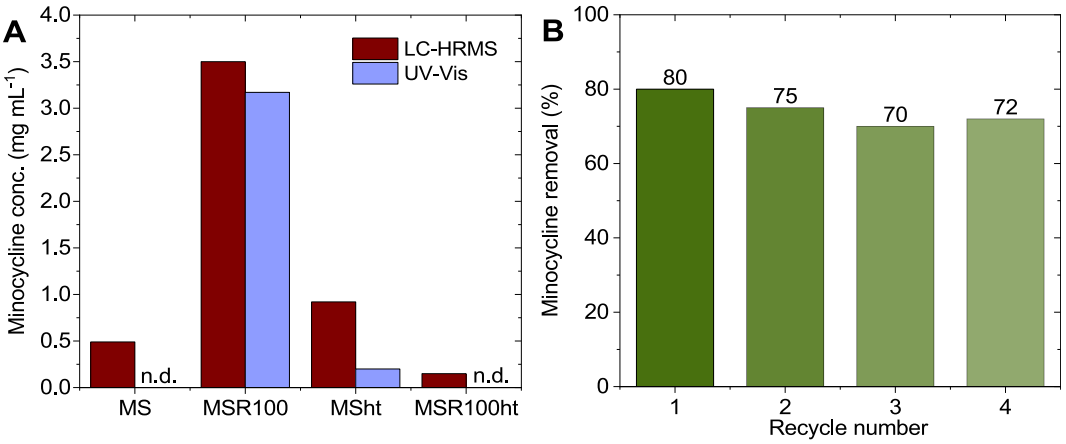

Fig. 6. Minocycline final concentration (mg•mL^{-1}) calculated through MS and UV–Vis, n.d. = not detected (A); minocycline's removal by MSR100ht achieved over 4 cycles. Each cycle is carried out using 50 mL of a 10 mg•L^{-1} minocycline solution and 50 mg of MSR100ht, at the constant temperature of 19 °C and stirring speed of 300 rpm. Each cycle lasts 90 min during which the solution is irradiated at the intensity of 1 sun (B).

degradation product (TP431) providing further proof of minocycline's degradation. Lastly, the best performing sample, MSR100ht, was tested over four photodegradation cycles, exhibiting high and overall stable removal percentages. Although the photodegradation tests were carried out in simple water matrices and further studies are needed to validate the applicability of the proposed system in real environments, the results here presented demonstrate the potential of linking the research on innovative systems for water remediation with the demanding need to valorise residues in the context of circular economy, thus opening an interesting upcycling pathway towards the generation of a new class of solar-driven photocatalysts.

CRediT authorship contribution statement

Francesca Langiano: Writing – original draft, Validation, Investigation, Data curation. **Sofia Moreira Fernandes:** Writing – review & editing, Validation, Investigation. **Beatriz Trindade Barrocas:** Writing – review & editing, Validation. **Anna Del Tedesco:** Writing – review & editing, Investigation, Data curation. **Pietro Riello:** Validation, Formal analysis. **Maria João Ferreira:** Validation, Investigation, Formal analysis. **Ana C. Marques:** Writing – review & editing, Supervision, Resources, Methodology, Funding acquisition. **Massimo Sgarzi:** Writing – review & editing, Supervision, Formal analysis, Data curation, Conceptualization. **Matteo Gigli:** Writing – review & editing, Resources, Project administration, Methodology, Funding acquisition, Formal analysis, Data curation, Conceptualization. **Claudia Crestini:** Writing – review & editing, Resources, Funding acquisition, Formal analysis.

Declaration of competing interest

The authors declare that they have no known competing financial interests or personal relationships that could have appeared to influence the work reported in this paper.

Acknowledgements

This study was carried out in the framework of the TURBOPACK Project (CUP N. H53D23007900001) (Mission 4 Component 2 Investment 1.1) funded by the European Union Next-GenerationEU – National Recovery and Resilience Plan (NRRP) – Fondo per il Programma Nazionale di Ricerca e Progetti di Rilevante Interesse Nazionale (PRIN). This manuscript reflects only the authors' views and opinions, neither the European Union nor the European Commission can be considered responsible for them.

The authors gratefully acknowledge Fundação para a Ciência e a Tecnologia (FCT) through the support of CERENA (Strategic Project FCT-UIDB/04028/2020), the FCT grant number 2022.09822.BD (SMF), the FCT project http://doi.org/10.54499/PTDC/EQU-EQU/1056/2020 (SOLAR2CLEAN—Engineered solar light driven photocatalytic systems for wastewater purification). We would like also to acknowledge Dr. Mário Vale for the useful discussions and suggestions regarding the MICROSCAFS® synthesis and M.Sc. Isabel Nogueira for acquiring the SEM images.

Appendix A. Supplementary data

RHA characterization: FT-IR spectrum, XRD diffractogram, thermogravimetric curve, elemental analysis data; MICROSCAFS® characterization: ATR-FTIR spectra, deconvoluted ^{29}Si MAS spectra, SEM and LDA size distribution, isotherms and pore size distribution, XRD diffractograms; adsorption isotherms and adsorption kinetic curves of minocycline; photodegradation kinetic curves and UV-Vis absorption spectra; chemical structure of minocycline and of the main degradation product (TP431). Supplementary data to this article can be found online at https://doi.org/10.1016/j.jwpe.2025.107003.

Data availability

Data will be made available on request.

References

[1] K. Fouad, M. Bassyouni, M.G. Alalm, M.Y. Saleh, Recent developments in recalcitrant organic pollutants degradation using immobilized photocatalysts, Appl. Phys. A Mater. Sci. Process. 127 (2021) 1–28, https://doi.org/10.1007/s00339-021-04724-1.
[2] D.G.J. Larsson, C.F. Flach, Antibiotic resistance in the environment, Nat. Rev. Microbiol. 20 (2022) 257–269, https://doi.org/10.1038/s41579-021-00649-x.
[3] J. Davies, D. Davies, Origins and evolution of antibiotic resistance, Microbiol. Mol. Biol. Rev. 74 (2010) 417–433, https://doi.org/10.1128/mmbr.00016-10.
[4] P.R. Rout, T.C. Zhang, P. Bhunia, R.Y. Surampalli, Treatment technologies for emerging contaminants in wastewater treatment plants: a review, Sci. Total Environ. 753 (2021) 141990, https://doi.org/10.1016/j.scitotenv.2020.141990.
[5] D. Kanakaraju, B.D. Glass, M. Oelgemöller, Titanium dioxide photocatalysis for pharmaceutical wastewater treatment, Environ. Chem. Lett. 12 (2014) 27–47, https://doi.org/10.1007/s10311-013-0428-0.
[6] K. Hashimoto, H. Irie, A. Fujishima, TiO_2 photocatalysis: a historical overview and future prospects, Jpn. J. Appl. Phys. Part 1 – Regul. Pap. Short Notes Rev. Pap. 44 (2005) 8269–8285, https://doi.org/10.1143/JJAP.44.8269.
[7] S. Wu, H. Hu, Y. Lin, J. Zhang, Y.H. Hu, Visible light photocatalytic degradation of tetracycline over TiO_2, Chem. Eng. J. 382 (2020) 122842, https://doi.org/10.1016/j.cej.2019.122842.
[8] S. Peiris, H.B. de Silva, K.N. Ranasinghe, S.V. Bandara, I.R. Perera, Recent development and future prospects of TiO_2 photocatalysis, J. Chin. Chem. Soc. 68 (2021) 738–769, https://doi.org/10.1002/jccs.202000465.

[9] X.D. Zhu, Y.J. Wang, R.J. Sun, D.M. Zhou, Photocatalytic degradation of tetracycline in aqueous solution by nanosized TiO_2, Chemosphere 92 (2013) 925–932, https://doi.org/10.1016/J.CHEMOSPHERE.2013.02.066.

[10] M. Khanmohammadi, J. Rahbar Shahrouzi, F. Rahmani, Insights into mesoporous MCM-41-supported titania decorated with CuO nanoparticles for enhanced photodegradation of tetracycline antibiotic, Environ. Sci. Pollut. Res. 28 (2021) 862–879, https://doi.org/10.1007/s11356-020-10546-0.

[11] L. Zhao, J. Yu, B. Cheng, Preparation and characterization of SiO_2/TiO_2 composite microspheres with microporous SiO_2 core/mesoporous TiO_2 shell, J. Solid State Chem. 178 (2005) 1818–1824, https://doi.org/10.1016/j.jssc.2005.03.024.

[12] J.B. Yoo, H.J. Yoo, B.W. Lim, K.H. Lee, M.H. Kim, D. Kang, N.H. Hur, Controlled synthesis of monodisperse SiO_2-TiO_2 microspheres with a yolk-shell structure as effective photocatalysts, ChemSusChem 5 (2012) 2334–2340, https://doi.org/10.1002/cssc.201200463.

[13] S. Permpoon, M. Houmard, D. Riassetto, L. Rapenne, G. Berthomé, B. Baroux, J. C. Joud, M. Langlet, Natural and persistent superhydrophilicity of SiO_2/TiO_2 and TiO_2/SiO_2 bi-layer films, Thin Solid Films 516 (2007) 957–966, https://doi.org/10.1016/j.tsf.2007.06.005.

[14] M. Vale, M.V. Loureiro, M.J. Ferreira, A.C. Marques, Silica-based microspheres with interconnected macroporosity by phase separation, J. Solgel Sci. Technol. 95 (2020) 746–759, https://doi.org/10.1007/s10971-020-05257-4.

[15] A.C. Marques, M. Vale, Macroporosity control by phase separation in sol-gel derived monoliths and microspheres, Mater 14 (2021) 4247, https://doi.org/10.3390/ma14154247.

[16] A.C. Marques, M. Vale, D. Vicente, M. Schreck, E. Tervoort, M. Niederberger, Porous silica microspheres with immobilized titania nanoparticles for in-flow solar-driven purification of wastewater, Global Chall. 5 (2021) 2000116, https://doi.org/10.1002/gch2.202000116.

[17] M. Vale, S. Orišková, A. Mariquito, L. Reis, M. Pinto, A.C. Marques, Multicomponent oxide microspheres with designed macroporosity (MICROSCAFS®): a customized platform for chemicals immobilization, RSC Adv. 13 (2023) 12951–12965, https://doi.org/10.1039/d3ra00895a.

[18] M. Vale, B.T. Barrocas, R.M.N. Serôdio, M.C. Oliveira, J.M. Lopes, A.C. Marques, Robust photocatalytic MICROSCAFS® with interconnected macropores for sustainable solar-driven water purification, Int. J. Mol. Sci. 25 (2024) 5958, https://doi.org/10.3390/ijms25115958.

[19] S. Rasalingam, R. Peng, R.T. Koodali, Removal of hazardous pollutants from wastewaters: applications of TiO_2-SiO_2 mixed oxide materials, J. Nanomater. 1 (2014) (2014) 617405, https://doi.org/10.1155/2014/617405.

[20] P.K. Jaseela, K.O. Shamsheera, A. Joseph, Mesoporous titania-silica nanocomposite as an effective material for the degradation of Bisphenol A under visible light, J. Saudi Chem. Soc. 24 (2020) 651–662, https://doi.org/10.1016/J.JSCS.2020.05.004.

[21] C. Priefer, J. Jörissen, O. Frör, Pathways to shape the bioeconomy, Resour 6 (2017) 10, https://doi.org/10.3390/resources6010010.

[22] D.M. Juela, Promising adsorptive materials derived from agricultural and industrial wastes for antibiotic removal: a comprehensive review, Sep. Purif. Technol. 284 (2022) 120286, https://doi.org/10.1016/J.SEPPUR.2021.120286.

[23] I. Aranaz, A.R. Alcántara, M.C. Civera, C. Arias, B. Elorza, A.H. Caballero, N. Acosta, Chitosan: an overview of its properties and applications, Polymers 13 (2021) 3256, https://doi.org/10.3390/polym13193256.

[24] M.S. Rostami, M.M. Khodaei, E. Benassi, Surface modified of chitosan by TiO_2@MWCNT nanohybrid for the efficient removal of organic dyes and antibiotics, Int. J. Biol. Macromol. 274 (2024) 133382, https://doi.org/10.1016/J.IJBIOMAC.2024.133382.

[25] Buhani, J.S. Dewi, N.S. Fajriyah, M. Rilyanti, Suharso, Sumadi, K.Z. Elwakeel, Modification of non-activated carbon from rubber fruit shells with 3-(aminopropyl)-triethoxysilane and its adsorption study on Coomassie brilliant blue and methylene blue in solution, Water Air Soil Pollut. 234 (2023) 1–13, https://doi.org/10.1007/s11270-023-06506-2.

[26] Buhani, Suharso, M. Rilyanti, F.D.R. Antika, L.P. Lestari, M. Ansori Sumadi, K. Z. Elwakeel, Functionalization of carbon from rubber fruit shells (*Hevea brasiliensis*) with silane agents and its application to the adsorption of bi-component mixtures of methylene blue and crystal violet, Environ. Sci. Pollut. Res. 31 (2024) 39994–40007, https://doi.org/10.1007/s11356-023-28031-9.

[27] M. Alexandri, J.P. López-Gómez, A. Olszewska-Widdrat, J. Venus, Valorising agro-industrial wastes within the circular bioeconomy concept: the case of defatted rice bran with emphasis on bioconversion strategies, Fermentation 6 (2020) 42, https://doi.org/10.3390/fermentation6020042.

[28] Visualizing the world's biggest rice producers. https://www.visualcapitalist.com/worlds-biggest-rice-producers/, 2022. (Accessed 14 February 2024).

[29] I.J. Fernandes, D. Calheiro, A.G. Kieling, C.A.M. Moraes, T.L.A.C. Rocha, F. A. Brehm, R.C.E. Modolo, Characterization of rice husk ash produced using different biomass combustion techniques for energy, Fuel 165 (2016) 351–359, https://doi.org/10.1016/j.fuel.2015.10.086.

[30] R. Pode, Potential applications of rice husk ash waste from rice husk biomass power plant, Renew. Sust. Energ. Rev. 53 (2016) 1468–1485, https://doi.org/10.1016/j.rser.2015.09.051.

[31] Y. Chen, F. Wang, L. Duan, H. Yang, J. Gao, Tetracycline adsorption onto rice husk ash, an agricultural waste: its kinetic and thermodynamic studies, J. Mol. Liq. 222 (2016) 487–494, https://doi.org/10.1016/J.MOLLIQ.2016.07.090.

[32] J.A.S. Costa, V.H.V. Sarmento, L.P.C. Romão, C.M. Paranhos, Adsorption of organic compounds on mesoporous material from rice husk ash (RHA), Biomass Convers. Biorefinery 10 (2020) 1105–1120, https://doi.org/10.1007/s13399-019-00476-4.

[33] V.C. Niculescu, M.S. Raboaca, Efficient rice-husk-derived silica nanocatalysts for organic dye removal from water, Catalysts 11 (2021) 815, https://doi.org/10.3390/catal11070815.

[34] A. Alhadhrami, G.G. Mohamed, A.H. Sadek, S.H. Ismail, A.A. Ebnalwaled, A.S. A. Almalki, Behavior of silica nanoparticles synthesized from rice husk ash by the sol-gel method as a photocatalytic and antibacterial agent, Materials 15 (2022) 8211, https://doi.org/10.3390/ma15228211.

[35] A.M. Martins, J.M. Marto, J.L. Johnson, E.M. Graber, A review of systemic minocycline side effects and topical minocycline as a safer alternative for treating acne and rosacea, Antibiotics 10 (2021) 757, https://doi.org/10.3390/antibiotics10070757.

[36] A. Rezaei, A. Moqadami, M. Khalaj-Kondori, Minocycline as a prospective therapeutic agent for cancer and non-cancer diseases: a scoping review, Naunyn Schmiedeberg's Arch. Pharmacol. 397 (2024) 2835–2848, https://doi.org/10.1007/s00210-023-02839-1.

[37] S. Rodriguez-Mozaz, I. Vaz-Moreira, S.V. Della Giustina, M. Llorca, D. Barceló, S. Schubert, T.U. Berendonk, I. Michael-Kordatou, D. Fatta-Kassinos, J.L. Martinez, C. Elpers, I. Henriques, T. Jaeger, T. Schwartz, E. Paulshus, K. O'Sullivan, K.M. M. Pärnänen, M. Virta, T.T. Do, F. Walsh, C.M. Manaia, Antibiotic residues in final effluents of European wastewater treatment plants and their impact on the aquatic environment, Environ. Int. 140 (2020) 105733, https://doi.org/10.1016/j.envint.2020.105733.

[38] J. Antos, M. Piosik, D. Ginter-Kramarczyk, J. Zembrzuska, I. Kruszelnicka, Tetracyclines contamination in European aquatic environments: a comprehensive review of occurrence, fate, and removal techniques, Chemosphere 353 (2024) 141519, https://doi.org/10.1016/j.chemosphere.2024.141519.

[39] J. Lyu, J. Shao, Y. Wang, Y. Qiu, J. Li, T. Li, Y. Peng, F. Liu, Construction of a porous core-shell homojunction for the photocatalytic degradation of antibiotics, Chem. Eng. J. 358 (2019) 614–620, https://doi.org/10.1016/j.cej.2018.10.085.

[40] L. Chen, S. Yang, Y. Huang, B. Zhang, F. Kang, D. Ding, T. Cai, Degradation of antibiotics in multi-component systems with novel ternary AgBr/Ag_3PO_4@natural hematite heterojunction photocatalyst under simulated solar light, J. Hazard. Mater. 371 (2019) 566–575, https://doi.org/10.1016/j.jhazmat.2019.03.038.

[41] P. Riello, P. Canton, G. Fagherazzi, Quantitative phase analysis in semicrystalline materials using the Rietveld method, J. Appl. Crystallogr. 31 (1998) 78–82, https://doi.org/10.1107/S0021889897009631.

[42] P. Riello, P. Canton, N. Comelato, S. Polizzi, M. Verità, G. Fagherazzi, H. Hofmeister, S. Hopfe, Nucleation and crystallization behavior of glass-ceramic materials in the $Li_2O{\pm}Al_2O_3{\pm}SiO_2$ system of interest for their transparency properties, J. Non-Cryst. Solids 288 (2001) 127–139, https://doi.org/10.1016/S0022-3093(01)00518-X.

[43] B.E. Warren, B.L. Averbach, The effect of cold-work distortion on X-ray patterns, J. Appl. Phys. 21 (1950) 595–599, https://doi.org/10.1063/1.1699713.

[44] X. Guo, J. Wang, Comparison of linearization methods for modeling the Langmuir adsorption isotherm, J. Mol. Liq. 296 (2019) 111850, https://doi.org/10.1016/j.molliq.2019.111850.

[45] T.H. Tran, A.H. Le, T.H. Pham, D.T. Nguyen, S.W. Chang, W.J. Chung, D. D. Nguyen, Adsorption isotherms and kinetic modeling of methylene blue dye onto a carbonaceous hydrochar adsorbent derived from coffee husk waste, Sci. Total Environ. 725 (2020) 138325, https://doi.org/10.1016/j.scitotenv.2020.138325.

[46] LCS-100 series small area solar simulators. https://www.newport.com/medias/sys_master/software/software/h18/h2a/9762949103646/LCS-100-DS-021821.pdf. (Accessed 23 July 2024).

[47] D. Tharani, M. Ananthasubramanian, Influence of pre-treatment processes on the purity and characteristics of silica extracted from rice husk, Biomass Conv. Bioref. 14 (2024) 12517–12529, https://doi.org/10.1007/s13399-022-03728-y.

[48] T.G. Korotkova, S.J. Ksandopulo, A.P. Donenko, S.A. Bushumov, A.S. Danilchenko, Physical properties and chemical composition of the rice husk and dust, Orient. J. Chem. 32 (2016) 3213–3219, https://doi.org/10.13005/ojc/320644.

[49] T.N. Tran, T.V.A. Pham, M.L.P. Le, T.P.T. Nguyen, V.M. Tran, Synthesis of amorphous silica and sulfonic acid functionalized silica used as reinforced phase for polymer electrolyte membrane, Adv. Nat. Sci. Nanosci. Nanotechnol. 4 (2013) 045007, https://doi.org/10.1088/2043-6262/4/4/045007.

[50] L. Vlaev, P. Petkov, A. Dimitrov, S. Genieva, Cleanup of water polluted with crude oil or diesel fuel using rice husks ash, J. Taiwan Inst. Chem. Eng. 42 (2011) 957–964, https://doi.org/10.1016/j.jtice.2011.04.004.

[51] P. Chen, W. Gu, W. Fang, X. Ji, R. Bie, Removal of metal impurities in rice husk and characterization of rice husk ash under simplified acid pretreatment process, Environ. Prog. Sustain. 36 (2017) 830–837, https://doi.org/10.1002/ep.12513.

[52] M. Colilla, M. Martínez-Carmona, S. Sánchez-Salcedo, M.L. Ruiz-González, J. M. González-Calbet, M. Vallet-Regí, A novel zwitterionic bioceramic with dual antibacterial capability, J. Mater. Chem. B 2 (2014) 5639–5651, https://doi.org/10.1039/C4TB00690A.

[53] D.J. Lieftink, B.G. Dekker, J.W. Geus, The structure of silica particles prepared by acid treatment of olivine: a nitrogen-physisorption and ^{29}Si-MAS NMR study, Stud. Surf. Sci. Catal. 118 (1998) 755–761, https://doi.org/10.1016/S0167-2991(98)80243-7.

[54] R.M. Almeida, Spectroscopy and structure of sol-gel systems, J. Solgel Sci. Technol. 13 (1998) 51–59, https://doi.org/10.1023/A:1008643019875.

[55] M. Riazian, N. Montazeri, E. Biazar, Nano structural properties of TiO_2-SiO_2, Orient. J. Chem. 27 (2011) 903–910.

[56] T. Mahalingam, C. Selvakumar, E. Ranjith Kumar, T. Venkatachalam, Structural, optical, morphological and thermal properties of TiO_2-Al and TiO_2-Al_2O_3 composite powders by ball milling, Phys. Lett. A 381 (2017) 1815–1819, https://doi.org/10.1016/J.PHYSLETA.2017.02.053.

[57] V.G. Erkov, S.F. Devyatova, E.L. Molodstova, T.V. Malsteva, U.A. Yanovskii, Si-TiO_2 interface evolution at prolonged annealing in low vacuum or N_2O ambient, Appl. Surf. Sci. 116 (2000) 51–56, https://doi.org/10.1016/S0169-4332(00)00415-3.
[58] J.Y. Zhang, I.W. Boyd, B.J. O'Sullivan, P.K. Hurley, P.V. Kelly, J.P. Sénateur, Nanocrystalline TiO_2 films studied by optical, XRD and FTIR spectroscopy, J. Non-Cryst. Solids 303 (2002) 134–138, https://doi.org/10.1016/S0022-3093(02)00973-0.
[59] B. Guo, H. Shen, K. Shu, Y. Zeng, W. Ning, The study of the relationship between pore structure and photocatalysis of mesoporous TiO_2, J. Chem. Sci. 121 (2009) 317–321, https://doi.org/10.1007/s12039-009-0036-5.
[60] D.M. Tobaldi, A. Tucci, A.S. Škapin, L. Esposito, Effects of SiO_2 addition on TiO_2 crystal structure and photocatalytic activity, J. Eur. Ceram. Soc. 30 (2010) 2481–2490, https://doi.org/10.1016/j.jeurceramsoc.2010.05.014.
[61] R. Saadi, Z. Saadi, R. Fazaeli, N.E. Fard, Monolayer and multilayer adsorption isotherm models for sorption from aqueous media, Korean J. Chem. Eng. 32 (2015) 787–799, https://doi.org/10.1007/s11814-015-0053-7.
[62] J. Chen, G. Li, Z. He, T. An, Adsorption and degradation of model volatile organic compounds by a combined titania-montmorillonite-silica photocatalyst, J. Hazard. Mater. 190 (2011) 416–423, https://doi.org/10.1016/j.jhazmat.2011.03.064.
[63] J.P.S. Valente, P.M. Padilha, A.O. Florentino, Studies on the adsorption and kinetics of photodegradation of a model compound for heterogeneous photocatalysis onto TiO_2, Chemosphere 64 (2006) 1128–1133, https://doi.org/10.1016/j.chemosphere.2005.11.050.
[64] C. Clementi, A. Cesaretti, B. Carlotti, F. Elisei, The role of pH in modulating the electronic state properties of minocycline drug and its inclusion within micellar carriers, J. Phys. Chem. A 120 (2016) 4994–5005, https://doi.org/10.1021/acs.jpca.5b12707.
[65] C. Kormann, M.R. Hoffmann, D.W. Bahnemann, Photolysis of chloroform and other organic molecules in aqueous TiO_2 suspensions, Environ. Sci. Technol. 25 (1991) 494–500, https://doi.org/10.1021/es00015a018.
[66] M. Brigante, P.C. Schulz, Remotion of the antibiotic tetracycline by titania and titania-silica composed materials, J. Hazard. Mater. 192 (2011) 1597–1608, https://doi.org/10.1016/j.jhazmat.2011.06.082.
[67] B. Ohtani, Photocatalysis A to Z - what we know and what we do not know in a scientific sense, J Photochem Photobiol C: Photochem Rev 11 (2010) 157–178, https://doi.org/10.1016/j.jphotochemrev.2011.02.001.
[68] C. Chen, W. Ma, J. Zhao, Semiconductor-mediated photodegradation of pollutants under visible-light irradiation, Chem. Soc. Rev. 39 (2010) 4206–4219, https://doi.org/10.1039/B921692H.
[69] C. Zhou, Y. Sun, F. Zhang, Y. Wu, Degradation of minocycline by the adsorption-catalysis multifunctional PVDF–PVP–TiO_2 membrane: degradation kinetics, photocatalytic efficiency, and toxicity of products, Int. J. Environ. Res. Public Health 18 (2021) 12339, https://doi.org/10.3390/ijerph182312339.